Solar Energy 170 (2018) 102–112

Contents lists available at ScienceDirect

Solar Energy

journal homepage: www.elsevier.com/locate/solener

Advanced characterization and in-situ growth monitoring of $Cu(In,Ga)Se_2$ thin films and solar cells

D. Abou-Ras*, M. Bär, R. Caballero[1], R. Gunder, C. Hages, M.D. Heinemann, C.A. Kaufmann, M. Krause, S. Levcenko, R. Mainz, J. Márquez, A. Nikolaeva, A. Redinger[2], N. Schäfer, S. Schorr, H. Stange, T. Unold, R.G. Wilks

Helmholtz-Zentrum Berlin für Materialien und Energie GmbH, Hahn-Meitner-Platz 1, 14109 Berlin, Germany

ARTICLE INFO

Keywords:
$Cu(In,Ga)Se_2$ solar cells
In-situ growth monitoring
Advanced characterization

ABSTRACT

The continuous improvement of $Cu(In,Ga)Se_2$ (CIGSe) solar cells relies considerably on advanced characterization of individual layers in the solar-cell stacks as well as of completed CIGSe devices. The present contribution provides an overview of corresponding efforts performed by various research groups at Helmholtz-Zentrum Berlin für Materialien und Energie GmbH. In-situ growth monitoring of CIGSe absorber layers by means of energy-dispersive X-ray spectrometry and light scattering is described, as well as structural analyses by means of X-ray and neutron diffraction. In addition, the characterization of surfaces and interfaces by soft X-ray and electron spectroscopy, the microscopic analysis by means of correlative electron microscopy, and optoelectronic characterization by optical spectroscopy are highlighted. The present contribution shows which substantial efforts in a research network are necessary in order to obtain deeper insight into materials properties and potentially limiting factors for the device performance, as well as to be able to control these factors during the solar-cell production.

1. Introduction

Thin-film solar cells based on $Cu(In,Ga)(S,Se)_2$ (CIGSSe) absorber layers have reached very high technological standard, with conversion efficiencies of almost 23% on laboratory-sized devices (Press release Solar Frontier, 2018a) and above 19% for industrially produced modules of $30 \times 30\,cm^2$ size (Press release Solar Frontier, 2018b). In spite of these achievements, the improvement of production processes for these solar cells still requires further knowledge about thin-film and phase formation as well as microstructure during the synthesis and thus, limitations in terms of reproducibility. Also, the optimization of thin films and their interfaces in the solar cell stacks remains an important issue for further improvements of the conversion efficiencies towards the 25% level and beyond.

Therefore, research in recent years at Helmholtz-Zentrum Berlin für Materialien und Energie GmbH (HZB) has focused on development of methods for the in-depth analysis of growth processes, mainly for $Cu(In,Ga)Se_2$ (CIGSe) thin films, based on light scattering, X-ray diffraction, and X-ray fluorescence. In addition, intensive work has also been conducted concerning the study of the (micro)structural, compositional as well as the electrical and optoelectronic properties of thin films and their interfaces, especially also when included in complete devices, on both, macroscopic (micrometers, millimeters) and microscopic (submicrometers) length scales. The present contribution will give an overview of these research efforts at HZB, with detailed examples of various methods for in-situ growth analysis as well as characterization of materials and devices.

2. In-situ monitoring of $Cu(In,Ga)Se_2$ growth

Deviations from the ideal band structure in a solar absorber layer, such as defect states in the band gap, can trap charge carriers and/or enhance recombination, thereby decreasing the power-conversion efficiency of the corresponding solar cell. Such electronic defects can originate from extended structural defects in the CIGSe absorber lattice or extrinsic dopants. In order to further improve the performance of CIGSe solar cells towards their theoretical limit, one of the key challenges is to understand the structural origins of electronic defects, their correlation to the optoelectronic properties of the CIGSe semiconductor thin film and to identify ways to eliminate these origins. A promising

* Corresponding author.
E-mail address: daniel.abou-ras@helmholtz-berlin.de (D. Abou-Ras).
[1] Current address: Universidad Autónoma de Madrid, Departamento de Física Aplicada, C/ Francisco Tomás y Valiente 7, 28049 Madrid, Spain.
[2] Current address: University of Luxembourg, 162a, avenue de la Faïencerie, L-1511 Luxembourg, Luxembourg.

https://doi.org/10.1016/j.solener.2018.04.032
Received 2 February 2018; Received in revised form 29 March 2018; Accepted 16 April 2018
Available online 19 May 2018
0038-092X/

approach to tackle this task is to analyze and correlate the time evolution of structural and optoelectronic properties during film deposition.

In-situ analysis by X-ray diffraction (XRD) and white light reflectometry (WLR) during the CIGSe absorber growth allows not only to detect planar defects, but offers the possibility to understand their formation and annihilation during thin film deposition (the reader is referred to reference Pistor et al. (2016) for an overview). Extended structural defects may affect the XRD patterns (Treacy et al., 1991), which makes them detectable in real time by in-situ XRD. Specifically, stacking faults of the 112 lattice planes and related planar defects can be detected by XRD through a characteristic broadening of the 112 diffraction peak with an additional maximum. This additional maximum is caused by the disturbance of the chalcopyrite symmetry (Rodriguez-Alvarez et al., 2013b; Mainz et al., 2016). Due to possible effects of texture it is not possible to exactly quantify the concentration of stacking faults detected by XRD. However, comparison with simulations show that already a concentration of a few percentages can lead to a signal of the magnitude observed experimentally (Mainz et al., 2016).

By ex-situ analysis it has been found that a high density of stacking faults is correlated with a reduced electron mobility (Stange et al., 2015). Additionally, theoretical calculations predict that dislocations at the edge of stacking faults may induce defects states in the band gap (Simsek Sanli et al., 2017).

Consequently stacking faults could also have an influence on the light absorption characteristics of CIGSe. Defects with energy states close to the band edge change the dependence of the absorption coefficient on the photon energy, introducing a so-called sub-bandgap tail which can be characterized by the sub-gap tail energy E_{SGT} (Heinemann et al., 2017). The E_{SGT} can be extracted from a fit of a WLR spectrum, making this parameter also accessible by real-time analysis (Heinemann et al., 2017).

It has previously been shown by a combination of real-time WLR and energy-dispersive XRD (EDXRD) that during the deposition of Cu-Se on a Cu-In-Ga-Se film (i.e., during the second stage of the 3-stage CIGSe co-evaporation process), the E_{SGT} decreases shortly before the film becomes Cu-saturated ([Cu]/([In] + [Ga]) = 1) (Heinemann et al., 2017). Additionally, it is known from real-time EDXRD measurements during CIGSe coevaporation that shortly before the film becomes Cu-saturated, planar defects in the CIGSe structure start to annihilate (Mainz et al., 2016; Stange et al., 2016). These results suggest a causality between these two observations. Whether this is really the case will be analyzed in the following.

Fig. 1 shows the experimental setup that allows to measure XRD and WLR in-situ during CIGSe deposition. A relative ratio of the Se to metal evaporation rates nominally > 3 was used in all processes.

In the WLR data for a process with 530 °C during the second and third stage (330 °C in the first stage) shown in Fig. 2a, pronounced interference fringes are visible, which are caused by the superposition of the reflection at the sample surface and the interface of the CIGSe layer with the molybdenum back contact. For the measurement, white light from a halogen lamp is focused on the substrate during film deposition. The reflected spectra shown in Fig. 2a were recorded by a Si-CCD and an InGaAs diode array with a time-resolution of one spectrum per second. Each spectrum was evaluated by fitting a calculated reflection spectrum to the measured spectrum. From the fit parameters the evolution of film roughness, the band gap and the sub-gap tail energy (E_{SGT}) were extracted. (For further details on the method see reference Heinemann et al. (2017).) The vertical lines in Fig. 2a marked 1 to 3, indicate (1) the beginning of the second process stage (Cu-Se deposition) and (2) the third process stage (In-Ga-Se deposition), as well as (3) the start of the cool down.

Simultaneously to the WLR data, real-time EDXRD datasets were recorded, which are depicted in Fig. 2b. By using a polychromatic synchrotron X-ray source, EDXRD and X-ray fluorescence data can be

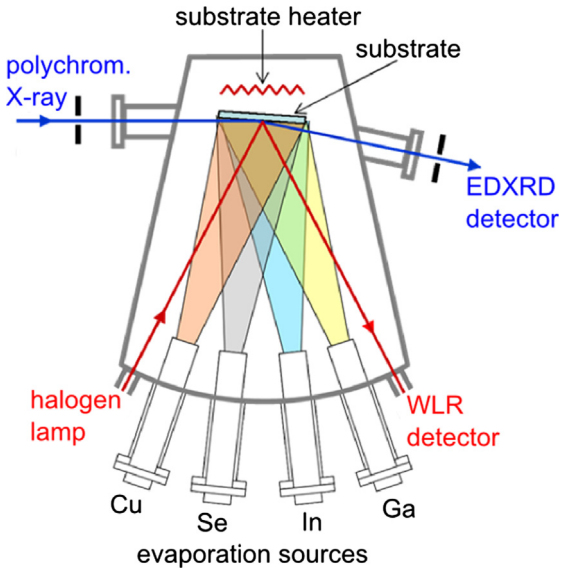

Fig. 1. Schematics of the coevaporation chamber for in-situ EDXRD and WLR measurements, attached to the synchrotron source BESSY (providing the polychromatic X-ray beam). See reference Heinemann et al. (2017).

acquired within a single spectrum recorded by means of an energy-dispersive detector during CIGSe film deposition (Rodriguez-Alvarez et al., 2013a). The EDXRD peaks in Fig. 2b show the phase evolution from γ-$(In,Ga)_2Se_3$ to γ-$Cu(In,Ga)_5Se_8$, β-$Cu(In,Ga)_3Se_5$, and α-$Cu(In,Ga)Se_2$ during Cu deposition. (For further details on the phase evolution, see references Rodriguez-Alvarez et al. (2013a), Pistor et al. (2015), Heinemann et al. (2017). During the Cu-rich ([Cu]/([In] + [Ga]) > 1) phase of the three-stage process, a $Cu_{2-x}Se$ diffraction peak can be identified. The moment in time of the Cu saturation can also be identified by a strong increase of the intensity of the Cu-K_α fluorescence signal (Fig. 2e), which is explained by the formation of Cu-Se on the growing film surface (Mainz et al., 2015). By comparing Fig. 2a and b, it can be seen that the phase transformations observed by EDXRD are related to the changes in the evolution of the WLR fringes (Heinemann et al., 2017). The average [Ga]/([Ga] + [In]) ratio in the final $Cu(In,Ga)Se_2$ film is 0.3, with a double gradient and a minimum [Ga]/([Ga] + [In]) ratio of 0.15, approximately 0.5–0.7 μm below surface.

The subgap-tail energy extracted from a fit of the WLR data is depicted in Fig. 2c. The figure shows a decrease of E_{SGT} shortly before the point of Cu saturation is reached. No E_{SGT} values are shown for the period where the composition of the thin film is Cu-rich, because the WLR data is affected by the presence of the secondary Cu-Se phase. When the thin film composition becomes Cu-poor ([Cu]/([In] + [Ga]) < 1) again during the third process stage, the E_{SGT} raises again to its original value.

With increasing Cu content, the intensity of the XRD signal associated with planar defects of the {1 1 2} lattice planes also decreases. This phenomenon is illustrated in Fig. 2d for a different process than in Fig. 1a and b with lower substrate temperature (420 °C) and a more pronounced defect signal. The planar defect signal vanishes abruptly at the beginning of the Cu-saturated stage, as determined by the increase of the Cu-K_α fluorescence signal (Fig. 2e). Contrary to the E_{SGT} value, however, the XRD planar defect signal does not increase again when the thin film composition becomes Cu-poor again.

The fact that the E_{SGT} returns to its previous value during the third stage of the deposition process while the planar defect XRD signal remains at noise level shows that the change of the E_{SGT} is not connected to the decrease of planar defects of the {1 1 2} lattice planes. The mirror-inverted development of the E_{SGT} shortly before and after the Cu-saturation point suggests a composition dependency. A possible

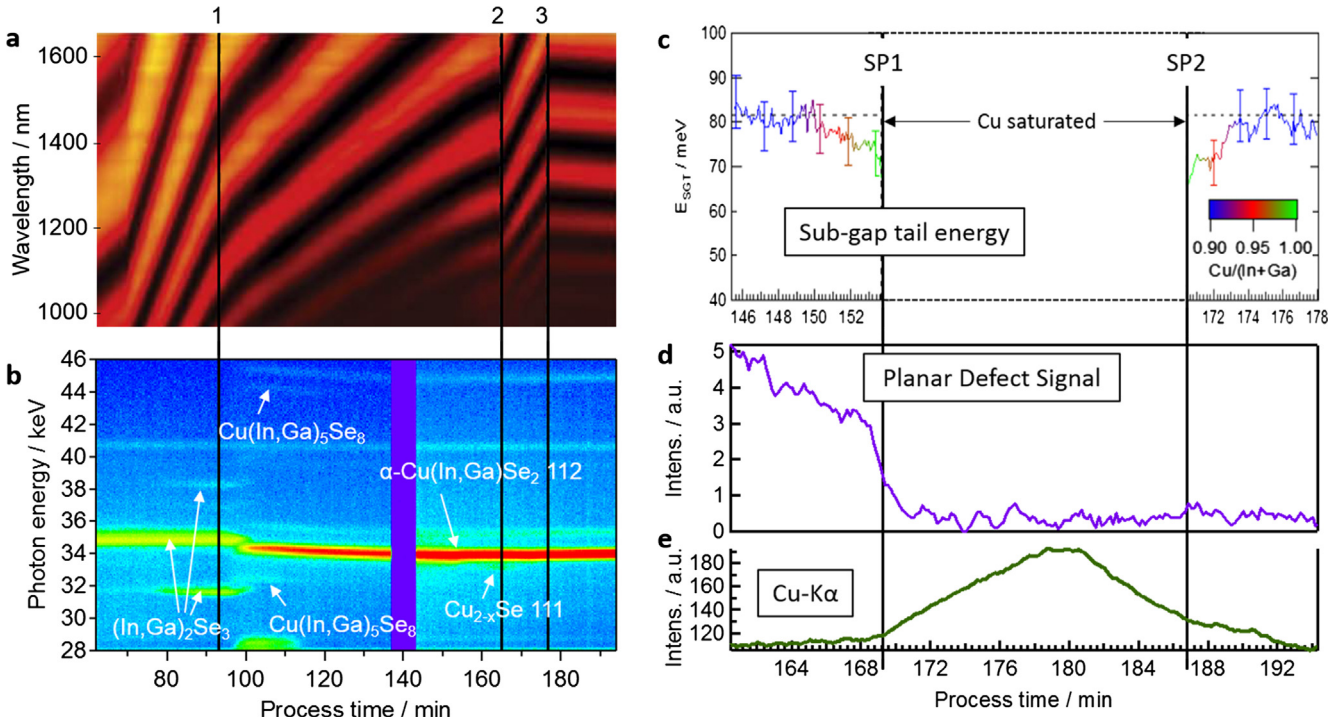

Fig. 2. Real-time analysis of optical and structural properties of a Cu-In-Ga-Se film during film deposition around the transitions from Cu-poor ([Cu]/([In] + [Ga]) < 1) to Cu-rich ([Cu]/([In] + [Ga]) > 1) and back from Cu-rich to Cu-poor composition. (a) WLR spectra recorded with a time resolution of 1 spectrum per second (at 530 °C substrate temperature). The vertical lines mark (1) the start of the Cu-Se deposition, (2) the start of the final In-Ga-Se deposition, and (3) the end of the deposition process. For the data of the complete process, see reference Heinemann et al. (2017). (b) EDXRD recorded simultaneously with the WLR data in a. The data collection was interrupted at around 140 min process time for 15 min owing to an electron injection at the synchrotron storage ring. (c) Sub-band tail energy extracted from WLR. (d) Evolution of planar defect signal extracted from EDXRD data recorded during CIGSe deposition at 420 °C substrate temperature. For more details, see references Mainz et al. (2016), Stange et al. (2016). (e) Intensity of the Cu-K_α fluorescence signal extracted from the same spectra as the planar defect signal in d.

explanation for this behavior could be that the increase of E_{SGT} is caused by point defects, which can be expected to become more numerous as the composition is more distant from the point of stoichiometry. While the annihilation of the planar defects seems to be non-reversible when changing the composition back to Cu-poor, point defects can be expected to be re-introduced in the CIGSe structure more easily, due to a low formation enthalpy and migration barrier of Cu vacancies (Pohl and Albe, 2010).

The measurements reported in the present Section show exemplary how the combination of *in-situ* analysis methods can be used to investigate possible correlations of structural defects with optoelectronic properties. The following Section provides insight into ex-situ, structural analyses of CIGSe thin films and powder specimens.

3. Structural properties of $Cu(In,Ga)Se_2$ thin films

For the analysis of crystal structures within thin-film materials, XRD is often the first choice. References Schorr et al. (2016), Gunder et al. (2017) give on overview of corresponding measurements using Bragg-Brentano or grazing-incidence (GI-XRD) configurations. When dealing with thin-film materials containing unknown phases, the investigation of crystal structure of the contained phases by Rietveld (1967) or Le Bail et al. (1988) refinement methods of the XRD or GI-XRD data (using possible solutions) is a very complex task; in some case, the refinement may even fail.

Instead, it is recommended to first determine phases (and their crystal structures) in powder samples from the same material systems. With the obtained crystal structures from powder diffraction experiments, refinement of the XRD data acquired on thin films often results in unambiguous solutions for the crystal structures contained in the thin films.

In addition, powder samples are also ideal for neutron scattering experiments, for which larger sample volumes (substantially larger than in thin films) are favored. From neutron scattering, it is possible to gather information on lattice-site occupations in crystal lattices and thus to conclude on favorable point defects. More specifically, the average neutron scattering lengths of lattice sites are changed by the presence of point defects in the lattice (e.g., vacancies or antisite defects) (Schorr et al., 2016). Stephan et al. (2011), Stephan and Scherb (2012) investigated defect concentrations with structural origin in nonstoichiometric $CuInSe_2$ and $CuGaSe_2$. These authors found that while in Cu-poor $CuInSe_2$, V_{Cu}, Cu_{In}, and In_{Cu} antisite defects are the most frequent ones, the dominant point defects in Cu-poor $CuGaSe_2$ are Ga_i and V_{Cu}. Stephan et al. (2016) investigated point defects in $CuInSe_2$ also in powder obtained by scratching off $CuInSe_2$ thin films from Mo/glass substrates. When studying the average neutron scattering lengths of Cu 4a and In 4b sites in $CuInSe_2$ containing / not containing Na, these authors show that in the presence of Na, Cu-poor $CuInSe_2$ thin films do not exhibit Cu_{In} antisite defects at high concentrations but rather V_{In}. The absence of high concentrations of antisite defects in (Cu-poor) $CuGaSe_2$ and Na-containing $CuInSe_2$ was interpreted in terms of a high structural ordering (Stephan et al., 2011; Stephan and Scherb, 2012).

Moreover, the presence of Na during growth was reported to affect the preferential orientation in polycrystalline $Cu(In,Ga)Se_2$ thin films (see, e.g., reference Rockett (2005)). The following study was conducted in order to shed more light on this issue. We emphasize that the results shown below were obtained on $CuInSe_2$ thin films from a low-temperature, three-stage growth process (300 °C during the In-Se deposition in the first stage and 480 °C during the Cu-Se and In-Se deposition in the second and third stages). The $CuInSe_2$ layer was deposited in the same process for all samples, which therefore have

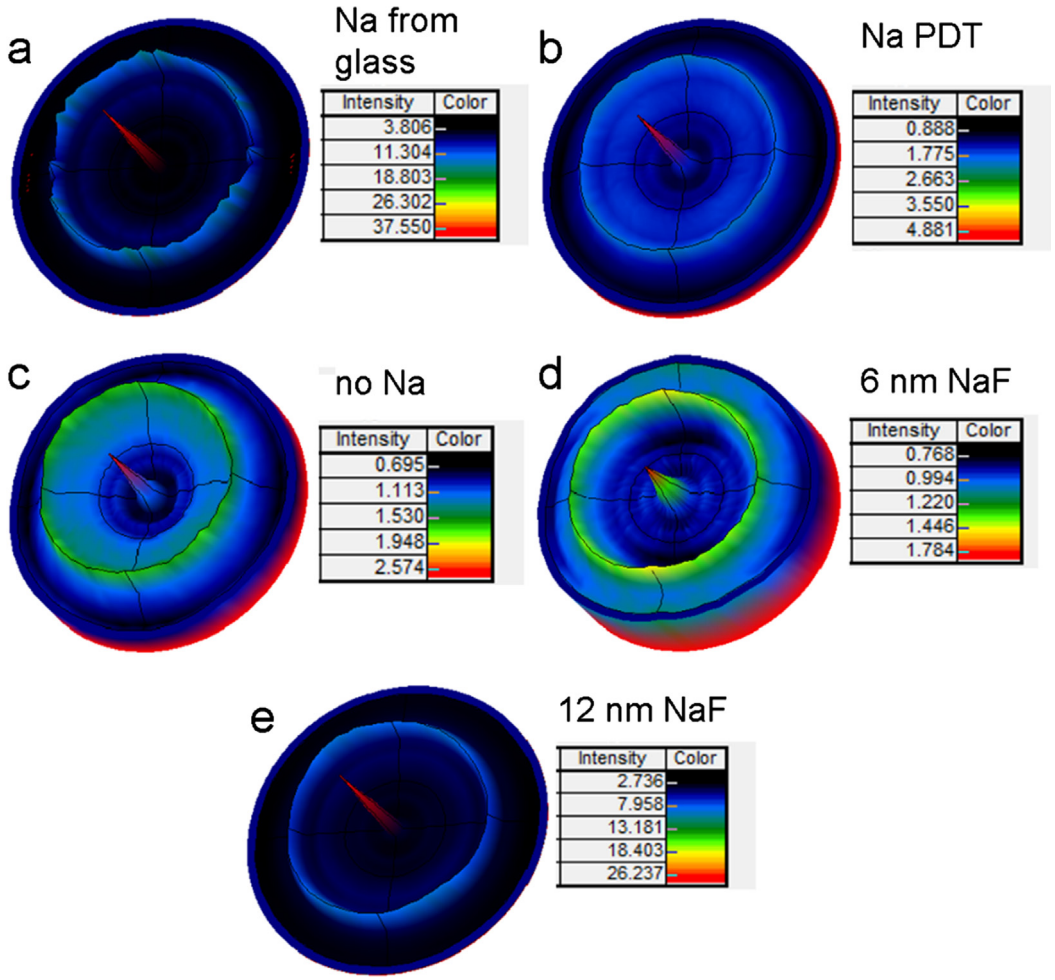

Fig. 3. Pole figures in {1 1 0} projection, extracted from XRD measurement of $CuInSe_2$ thin films into which Na was incorporated using different recipes. The $CuInSe_2$ layers were grown at 480 °C using a three-stage process. (a) Na diffusion from the soda-lime glass, (b) Na incorporated by a NaF post-deposition treatment at during sample cool-down right after $CuInSe_2$ deposition starting at 480 °C, (c) Na diffusion from the soda-lime glass impeded by a diffusion barrier layer (no Na, reference), (d) and (e) use of NaF precursor layers with thicknesses of 6 and 12 nm on top of the diffusion barrier layer.

nominally identical thickness. Na was introduced by diffusion from the soda-lime substrate, by a NaF precursor (thicknesses of 6 and 12 nm) deposited on the Mo/glass substrate (using a SiO_xN_y barrier on the glass to prevent Na diffusion), or by NaF post-deposition treatment (PDT) at 480 °C (also using a SiO_xN_y barrier on the glass) with a Se background pressure in the chamber. Fig. 3 shows the pole figures in {1 1 0} projection obtained by XRD and showing the characteristics of the preferred orientation in the $CuInSe_2$ thin films. All investigated films exhibit a preferred orientation in ⟨1 1 0⟩/⟨2 0 1⟩ direction. However, the magnitude of the film texture (given in multiples of random distribution) differ substantially and depend on the way of how Na was introduced (and presumably on the corresponding available Na during growth of the $CuInSe_2$ layer or during the PDT). It is apparent that Na diffusion from the soda-lime glass results in the strongest ⟨1 1 0⟩/⟨2 0 1⟩ texture (Fig. 3a). Simply applying a Na diffusion barrier between glass and Mo leads to a very weak preferential ⟨1 1 0⟩/⟨2 0 1⟩ orientation (Fig. 3c), which is not substantially improved by adding Na via PDT (Fig. 3b) or via a 6 nm thick NaF precursor layer (Fig. 3d). Only when increasing the thickness of the precursor layer to 12 nm, a strong ⟨1 1 0⟩/⟨2 0 1⟩ texture is obtained.

Although it was not possible to conclusively relate the obtained film textures to the used method of Na introduction, the XRD results shown in Fig. 3 are in good agreement with the ones provided by Rudmann (2004), who studied the preferred orientation of CIGSe thin films deposited at low substrate temperature (450 °C), however, only by comparing peak intensities obtained by XRD θ-2θ scans. A direct link between the preferential orientations in the $CuInSe_2$ (or $Cu(In,Ga)Se_2$) layers and the device performance of corresponding solar cells has been provided by Contreras et al. (2006) for CIGSe grown at elevated temperatures of about 580 °C, showing that CIGSe absorber layers with preferential ⟨1 1 0⟩/⟨2 0 1⟩ orientations outperform those with ⟨2 2 1⟩ texture owing to lower densities of nonradiative recombination centers.

In the following Section, advanced approaches for the analysis of surfaces and interfaces in the $Cu(In,Ga)Se_2$ solar-cell stack are provided.

4. Interfaces and surfaces

In order to reveal the (depth-resolved) chemical and electronic structures of surfaces and interfaces, a combination of *non-destructive* techniques, i.e., X-ray photoelectron spectroscopy (XPS) and soft X-ray emission spectroscopy (XES), deliberately varying the probing depth, as well as ultraviolet photoelectron spectroscopy (UPS) and inverse photoemission (IPES), probing occupied and unoccupied density of states can be employed (see reference Bär et al. (2016a) for an overview). In the following, a short review of our findings on In_2S_3 deposited on the CIGSe absorber by thermal co-evaporation of elemental indium and sulfur at elevated temperature (i.e., 200 °C) is presented to demonstrate how powerful this approach is. For higher conversion efficiencies and to facilitate industrial scale large-area production, it is desirable to replace the CdS buffer layer in the CIGSe-based device structure with a non-

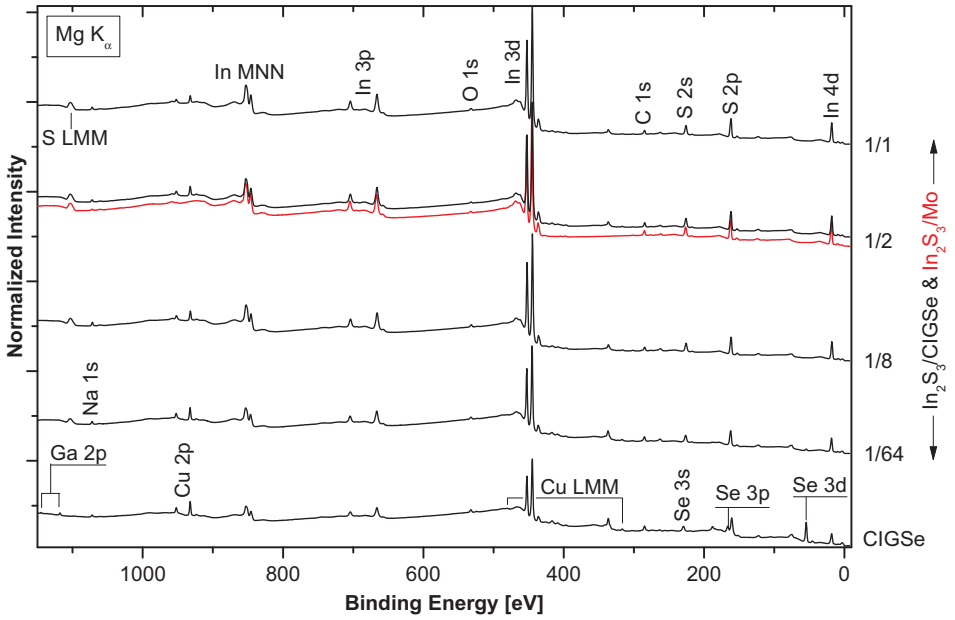

Fig. 4. XPS survey spectra of In_2S_3/CIGSe samples with increasing In_2S_3 buffer layer thickness (1/64 → 1/1). For comparison, the spectra of a bare CIGSe absorber (bottom) and a 1/2 In_2S_3/Mo reference sample (red solid line) are also shown. (For interpretation of the references to colour in this figure legend, the reader is referred to the web version of this article.)

toxic, more transparent buffer, and the conventionally used chemical bath buffer deposition with a technique suitable for in-line processing. For an insight-driven buffer layer optimization, a detailed knowledge of the chemical and electronic properties of the (buried) buffer/absorber is a prerequisite. In the present chapter, we provide as an example an extensive spectroscopic analysis of the "In_2S_3"/CIGSe interface structure in unprecedented detail (Bär et al., 2010, 2013, 2016b; Hauschild et al., 2015, in press). For more specifics (in particular with respect to details on the preparation and performance of the studied CIGSe absorbers), we refer to the original publications (Bär et al., 2010, 2013, 2016b).

Fig. 4 shows the XPS survey spectra of the "In_2S_3"/CIGSe samples with varying In_2S_3 thickness. "1/1" refers to the standard deposition time (10 min) relevant for solar cells devices resulting in a buffer thickness of approx. 80 nm. "1/2" (5 min), "1/8" (75 s), and "1/64" (10 s) gives the deposition times (as measure of thickness) related to the standard 10 min. For comparison, the spectra of the bare CIGSe absorber and the 1/2 In_2S_3/Mo reference sample are also shown. The spectra are discussed in detail in reference Bär et al. (2013). Briefly, we find significant differences in the attenuation trends of the Cu-, Ga-, Se-, and Na-related peaks. (Note that the Na stems from the soda-lime glass substrate that diffuses to and accumulates at the absorber surface owing to the elevated temperatures during absorber preparation, see, e.g., reference Song et al. (2012) and references therein for more details.)

Most prominently, while the Se 3d photoemission line vanishes even for the thinnest (1/64) overlayer (indicating a complete coverage of the CIGSe absorber by the deposited In_2S_3 buffer), Cu 2p and Na 1s peaks can still be clearly recognized even for the thickest In_2S_3 buffer layers. For Cu, this is particularly apparent when comparing the spectra of the two 1/2 In_2S_3 buffer layers deposited on CIGSe and Mo, respectively. These observations are confirmed by a thorough quantification (see reference Bär et al. (2010) for details), as depicted in Fig. 5, showing the XPS derived [Cu]/[In] ratio. In combination with the composition derived from S $L_{2,3}$ XES measurements (also indicated in Fig. 5; see reference Bär et al. (2010) for details), it results in the following picture: For the "In_2S_3"/CIGSe samples, we find similar XPS and XES [Cu]/[In] ratios for the thinnest and thickest layers, but not for the intermediate "In_2S_3" layers. The expected similar values for the thick samples are in agreement with a homogeneous $CuIn_5S_8$ composition throughout the entire buffer. S $L_{2,3}$ XES spectra only probe the chemical environment of the S atoms, and so only the S-containing $CuIn_5S_8$ compound (formed on a S-free CIGSe) contributes to the respective

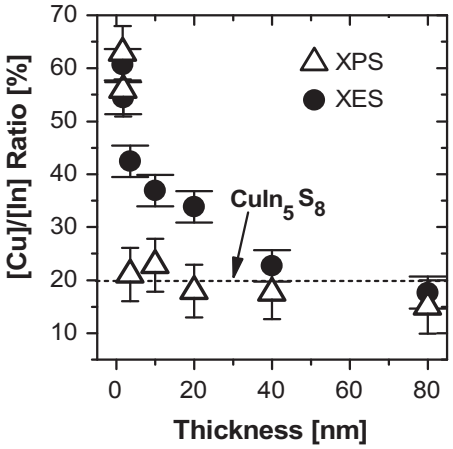

Fig. 5. Comparison of [Cu]/[In] ratios of an In_2Se_3 thickness series on CIGSe determined from XPS and XES. The [Cu]/[In] ratio of a $CuIn_5S_8$ compound is also indicated.

spectra. Assuming a homogeneous $CuIn_5S_8$ composition (i.e., no Cu gradient), the XES [Cu]/[In] ratio of all "In_2S_3"/CIGSe samples should thus be similar to that of the formed $CuIn_5S_8$ buffer compound. The observed deviation for low thicknesses is ascribed to the substitution of Se by S in the CIGSe surface/interface region during the first stages of the "In_2S_3" deposition, probably forming a $Cu(In,Ga)(S,Se)_2$ interlayer. The difference between the XPS and XES [Cu]/[In] ratios for the intermediate "In_2S_3" thicknesses is due to the different information depths of the techniques (more precisely: due to the inelastic mean free path $\lambda_{Cu\ 2p} \sim 1$ nm (QUASES-IMFP-TPP2M) of electrons and the much larger attenuation length of photons, here, approx. 30 nm (Henke et al. (1993)). In the early stages of the "In_2S_3" deposition, the buffer is thin enough that the (sulfurized) CIGSe side of the "In_2S_3"/CIGSe interface contributes significantly to both XPS and XES spectra, leading to high [Cu]/[In] ratios. Then, with increasing thickness, the contribution of the "In_2S_3"/CIGSe interface region is reduced, in particular for XPS. As a result, the XPS-derived ratio rapidly decreases to the $CuIn_5S_8$ level. Due to the larger information depth the XES spectra, in contrast, still contain a substantial contribution from the interface region. This results in a much slower decrease of the [Cu]/[In] ratio.

The schematics in Fig. 6 summarizes the findings of our XPS and

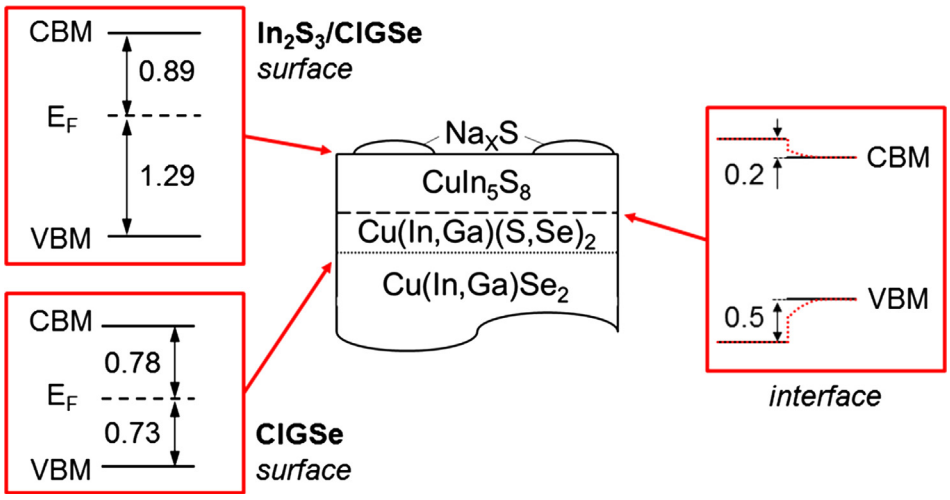

Fig. 6. Center panel: Simplified scheme of the proposed chemical structure of the surface region of a standard "In_2S_3"/CIGSe sample. Left panels: Presentation of the position of the VBM and CBM with respect to the Fermi level (E_F) for the surface of the bare CIGSe absorber (bottom) and the surface of the standard (1/1) "In_2S_3"/CIGSe sample. Right panel: Scheme of the energy level alignment at the In_2S_3/CIGSe interface.

XES investigations. We suggest that, during In_2S_3 co-evaporation at 200 °C on a CIGSe substrate, a $CuIn_5S_8$ buffer is formed, the absorber surface/interface region is chemically modified by a partial substitution of Se by S (probably resulting in a $Cu(In,Ga)(S,Se)_2$ interlayer), and Na and S accumulate at the sample surface, possibly forming Na_XS islands or a thin film. Acting as a Cu source for the $CuIn_5S_8$ formation, the CIGSe absorber near the interface will be Cu-depleted. All of these chemical "modifications" are expected to have a significant impact on the electronic structure at the interface and thus on the overall solar cell performance.

In order to specifically address this question, additional UPS and IPES measurements were performed. The position of the valence band maximum (VBM) and conduction band minimum (CBM) can be derived by linear approximation of the leading edge of the UPS and IPES spectrum, respectively. The determined values for the bare CIGSe absorber surface and the surface of the standard "In_2S_3"/CIGSe sample are depicted in the bottom-left and top-left panel in Fig. 6. Using these values, we find that the electronic surface band gap (E_g^{Surf} = CBM − VBM) of the CIGSe absorber is (1.51 ± 0.14) eV, which is significantly larger than the optical bulk band gap (approx. 1.1 eV, derived from the external quantum efficiency data in reference Barreau et al. (2006). A band gap widening towards the absorber surface was observed for high-efficiency chalcopyrites before (Tuttle et al., 1991; Schmid et al., 1993; Morkel et al., 2001; Bär et al., 2008, 2009) and is consistent with the Cu surface-deficiency found for the here-studied CIGSe sample (Bär et al., 2010, 2016b). For the standard "In_2S_3"/CIGSe sample, we find the E_g^{Surf} to be 2.18 (± 0.14) eV, which falls within the wide range of optically-derived bulk band gaps reported for In_2S_3 thin films deposited by dry methods: (1.98–2.32) eV in reference Madelung et al. and (2.0–2.7) eV in reference Barreau (2009). However, compared to the E_g^{Surf} value derived for a In_2S_3/Mo reference [2.45 (± 0.14) eV] sample, the electronic surface band gap for the "In_2S_3"/CIGSe sample is reduced. This smaller E_g^{Surf} is ascribed to the observed Cu diffusion from the absorber into the buffer layer and the associated formation of a $CuIn_5S_8$-like buffer composition (Bär et al., 2010, 2016b).

Based on the VBM and CBM values and taking interface-induced band bending into account (as described in detail in reference Bär et al. (2013) the energy level alignment at the "In_2S_3"/CIGSe interface was determined to form a cliff-like VB offset (VBO) of −0.5 (± 0.2) eV and a CB offset (CBO) of +0.2 (± 0.2) eV, i.e., a small spike, which is depicted in the right panel of Fig. 3. However, due to the significant Cu diffusion and the suggested partial S/Se substitution at the absorber surface, the modification of the electronic absorber structure by, e.g., the formation of a Cu-deficient $Cu(In,Ga)(S,Se)_2$-like absorber phase in the proximity of the "In_2S_3"/CIGSe interface is expected. Both effects lead to an increase of the absorber band gap at the interface (Zhang et al., 1998; Wei and Zunger, 1995) and "smear out" the offsets, as indicated by the red dotted lines. As a result the magnitude of the here-derived VBO and CBO can only be considered as upper bounds to the true values.

Device simulations (Niemegeers et al., 1995; Liu and Sites, 1996; Minemoto et al., 2001) predict that a flat or moderately spike-like CBO does not hinder the current transport across the buffer/absorber interface. Thus, the here-derived CBO upper bound values at the In_2S_3/CIGSe interface of + 0.2 (± 0.2) eV might thus still be in agreement with a band alignment suitable for high-efficiency thin-film solar cell devices

This example shows that in order to get a detailed picture of the materials, layer stacks, and interfaces, it is important to combine complementary characterization techniques. Furthermore, it is crucial to study the relevant interface (i.e., after it is formed) which can change due to postdeposition treatments and/or subsequent deposition/manufacturing steps, promoting in-system/in-situ experiments. In the following section, microscopy approaches for the analysis of $Cu(In,Ga)Se_2$ thin-film bulk properties and the corresponding relationships to device performances are provided.

5. Microscopic materials and device properties

In order to detect spatially inhomogeneous distributions of doping or composition (grain-to-grain or also gradients within individual grains), analysis tools with appropriate spatial resolutions are required. Scanning electron microscopy (SEM) and its related techniques can provide insight to various materials and device properties at scales ranging from few 10 nm up to several cm (Abou-Ras et al., 2016a). Apart from imaging, elemental distributions can be acquired by means of energy-dispersive X-ray spectrometry (EDXS). It is often wrongly assumed that EDXS in SEM features poor spatial resolutions (of about 1 μm) owing to high excitation volumes, and that for characterization of the layers in the $Cu(In,Ga)Se_2$ solar-cell stack in cross-section geometry, this technique is not useful. However, when using small acceleration voltages as well as (for mapping) low-energy X-ray lines, which exhibit a small mean-free path and thus a small information volume of the emitted X-rays, the corresponding EDXS elemental-distribution maps represent compositional information even for thin films with very small thicknesses (only few 10 nm). Fig. 7 gives an example of such EDXS elemental distribution maps acquired at 7 kV acceleration voltage, providing the Cd distribution even for the 50 nm thin CdS layer. For these EDXS analyses, the cross-section of a ZnO:Al/i-ZnO/CdS/CIGSe/Mo/glass stack was polished mechanically and by Ar-ion beams (the CIGSe layer was coevaporated using a three-stage process).

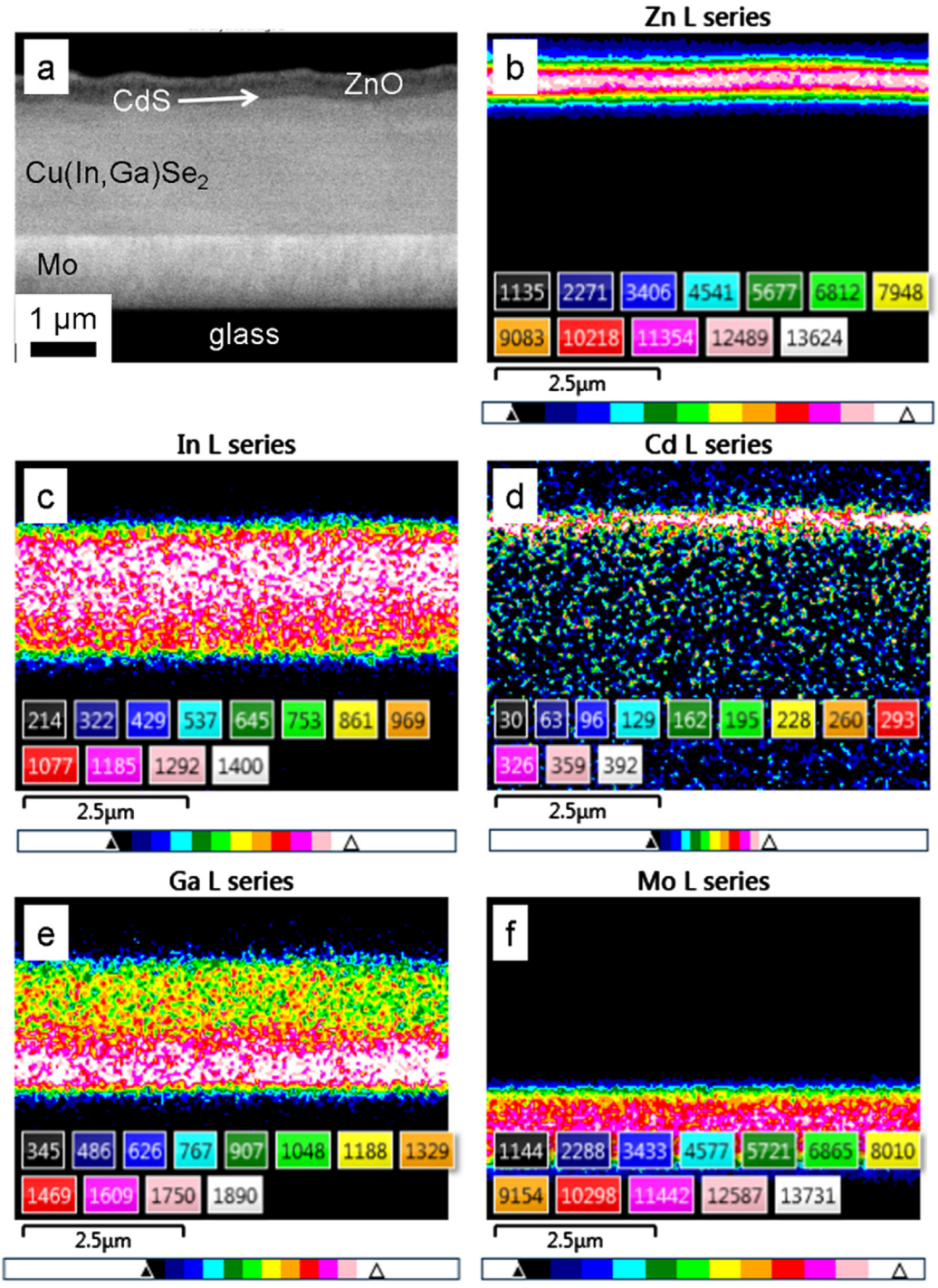

Fig. 7. Cross-sectional SEM image of a ZnO:Al/i-ZnO/CdS/Cu(In,Ga)Se_2/Mo/glass stack (a), and elemental distribution maps acquired at 7 kV acceleration voltage by EDXS from the same identical area, using the (b) Zn-L, (c) In-L, (d) Cd-L, (e) Ga-L, and (f) Mo-L X-ray lines. The false colors represent the net intensities (values provided by the legends in the subfigures). These EDXS results show the Ga gradient in the CIGSe layer and the capability of this technique to detect the elemental distributions also in the thin (50 nm) CdS layer.

Moreover, electron-backscatter diffraction (EBSD) probes the local crystal orientation and symmetry, and thus can provide grain-size and orientation distributions, and also allows for categorizing grain boundaries via the misorientations between neighboring grains with spatial resolutions ranging from about 10 nm when using electron-transparent lamellae up to several cm for bulk specimens (Kühnapfel et al., 2016). From the recorded EBSD patterns, also microstrain distributions within individual grains can be determined (Schäfer et al., 2016). Analysis of local short-circuit currents in Cu(In,Ga)Se_2 solar cells is possible by means of electron-beam-induced current measurements. Applying a corresponding model to EBIC profiles from cross-section specimens extracted perpendicular to the substrate provides values for the widths of the space-charge region w_{SCR} (linked to the doping of the Cu(In,Ga)Se_2 layer) as well as for the diffusion lengths in the quasi-neutral region of the Cu(In,Ga)Se_2 film (related to the lifetime of the electrons) (Nichterwitz et al., 2009). When using a beam-blanker in the microscope as well as a lock-in amplifier, the variation in w_{SCR} with varying applied voltage gives insight to the net doping density in the Cu

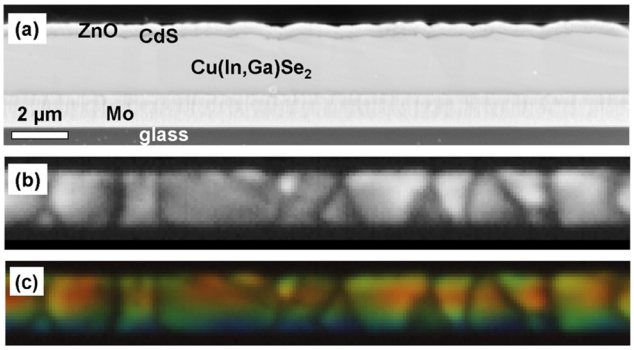

Fig. 8. SEM image (a) as well as CL intensity (b) and peak-wavelength distributions (c) acquired on the same identical position on a cross-section specimen prepared from a ZnO/CdS/CIGSe/Mo/glass stack. The CL measurements were performed at room temperature using a DELMIC SPARC system. The colors in subfigure c agree well with the band-gap energies expected from the local [Ga] values (blue: about 1.3 eV, yellow: about 1.2 eV, red: about 1.15 eV). (For interpretation of the references to colour in this figure legend, the reader is referred to the web version of this article.)

$(In,Ga)Se_2$ layer as well as the built-in potential of the diode (Abou-Ras et al., 2015).

Information on the radiative recombination at high spatial resolutions of down to below 100 nm is given by cathodoluminescence (CL) measurements. When applied on a cross-section specimen of a Cu $(In,Ga)Se_2$ solar cell, the corresponding CL map (Fig. 8) represents not only the microstructure via CL intensities decreased at grain boundaries, but also the Ga gradient via corresponding CL peak shifts.

This peak shift becomes more apparent when plotting the position on the cross-section as a function of the peak wavelength (Fig. 9). A corresponding distribution of the local band-gap energy E_g can be calculated from the Ga gradient measured by means of EDXS via $E_g(x) = (1 - x)E_g(CuInSe_2) + xE_g(CuGaSe_2) - bx(1 - x)$, where $x = [Ga]/([In] + [Ga])$ and b is the bowing factor ($b = 0.2$). Here, $E_g(CuInSe_2) = 1.04$ eV and $E_g(CuGaSe_2) = 1.68$ eV (Alonso et al., 2001) were used. It can be seen that the CL peak shift perpendicular to the substrate (Fig. 9a) agrees well with the corresponding distribution calculated from the Ga gradient (Fig. 9b).

Enhanced microscopic information can be gathered whenever several techniques are acquired on the same specimen area. Examples for such work include combination of EBSD, EBIC, and CL investigations in order to determine the recombination velocities at grain boundaries and their correlation with the characters of grain-boundary planes (Abou-Ras et al., 2016b), and the combination of EBSD and scanning probe microscopy in order to study barriers for charge carriers at grain boundaries (Baier et al., 2011). Recombination velocities and barrier heights for charge carriers at grain boundaries together exhibit important input parameters for two-dimensional device simulations, which indicate that enhanced recombination at CIGSe grain boundaries is one possible origin of the limited open-circuit voltage in the corresponding solar cells (Abou-Ras et al., 2016c).

A currently interesting research topic is the investigation of inhomogeneous EBIC and CL signal distributions in $Cu(In,Ga)Se_2$ thin films when comparing those acquired on adjacent grains (the reader is referred to a recent review on this topic, see reference Abou-Ras et al. (2018). These inhomogeneities can limit the open-circuit voltage of the corresponding solar cells (Rau and Werner, 2004) and can be attributed mainly to local fluctuations in the net doping (present probably due to inhomogeneous distributions of charged point defects) and in the lifetime of the electrons (which may be, e.g., affected by inhomogeneous distributions of line or planar defects within grains, which contribute to enhanced recombination) (Stephan et al., 2016). These electrical and optoelectronic analyses on the sub-micrometer scale are correlated with corresponding macroscopic measurements, which are outlined in the following Section.

6. Optical spectroscopy

Hyperspectral imaging techniques have the potential to provide information regarding the optoelectronic properties of materials and devices with spatial resolution (Unold and Gütay, 2016; Oliva et al., 2016). In contrast to conventional luminescence spectroscopy measurements where the emitted light is collected from a single spot, hyperspectral imaging luminescence offers the possibility to acquire spatially-resolved luminescence maps within a single measurement cycle where the whole sample is illuminated homogeneously. By doing so, the optoelectronic properties of absorber layers and full devices can be mapped by means of photo- and electroluminescence. For electroluminescence, a complete device structure is required to inject current. In photoluminescence, no contact layers are required and bare absorber layers can also be measured with or without functional layers; such analysis allows for the systematic probing of radiative recombination rates at the various stages of device fabrication (e.g. bare absorbers, absorber/buffer, and completed device) all by means of optical spectroscopy. Luminescence images are generally collected with a Si-CCD or InGaAs-based camera depending on the spectral region of the emission

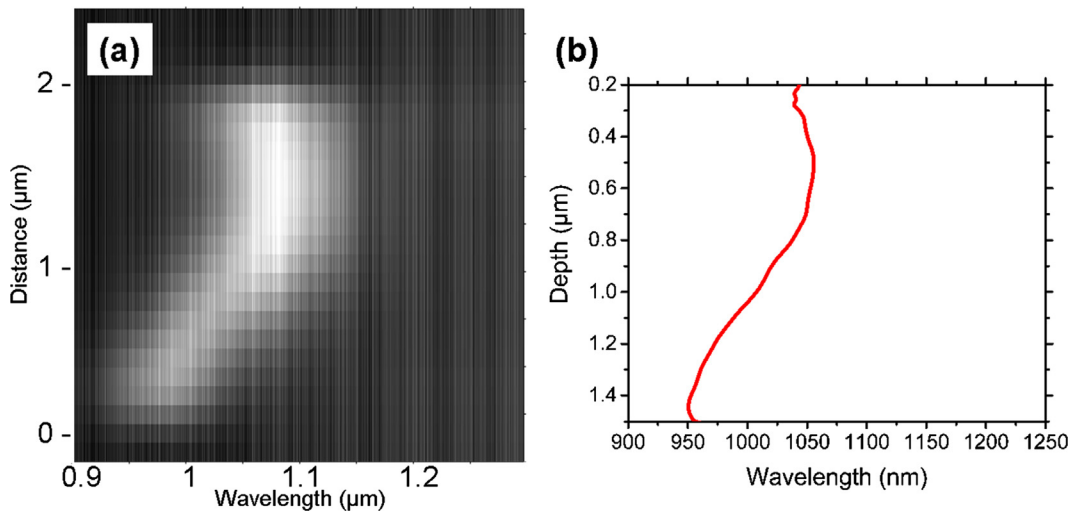

Fig. 9. (a) CL spectra extracted from the CL spectral image, along a line perpendicular to the substrate, and plotted against the distance. This linescan is in very good agreement with the distribution of the band-gap wavelength calculated from the Ga distribution measured by EDXS (b).

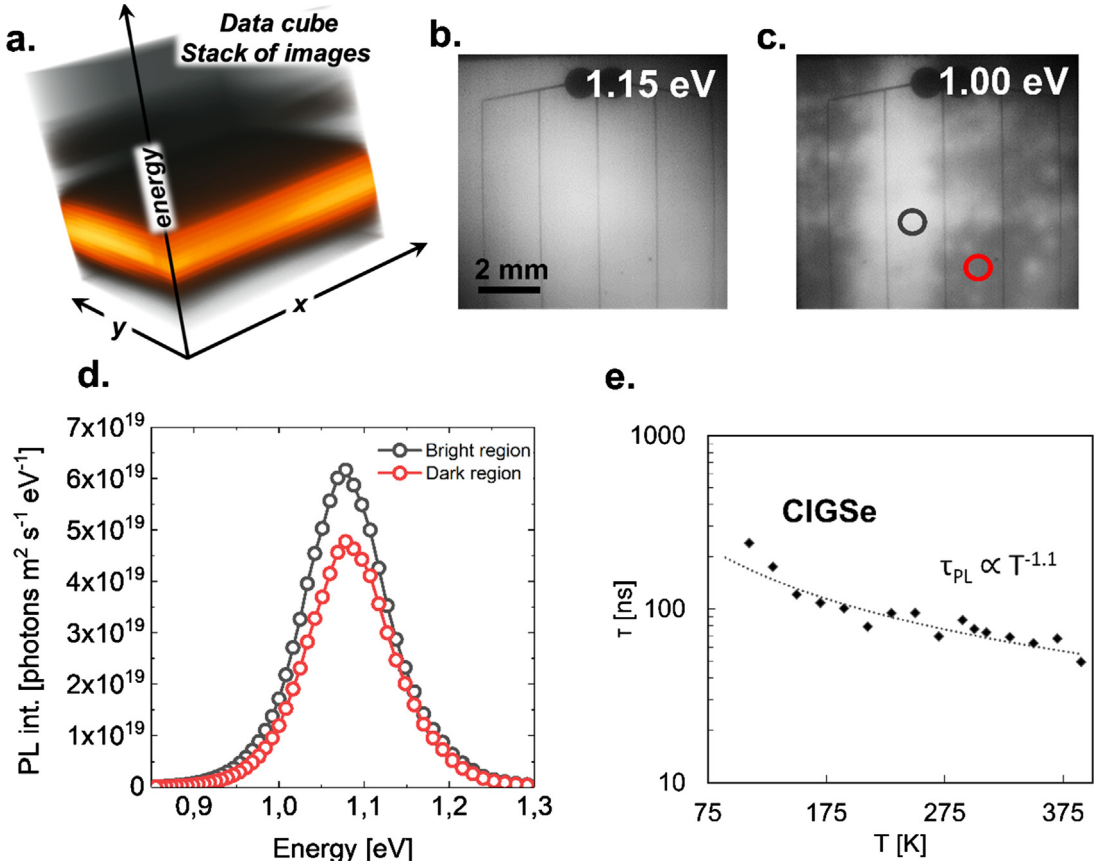

Fig. 10. (a) Schematics representation of the hyperspectral 3D data cube. PL images of a CIGSe solar cell at emission energies of 1.15 eV (b) and 1.00 eV (c) (intensity variations in the image corners are affected by aberration in the detection optics). (d) PL spectra of integrated over the dark and bright areas represented by black and red circles in (c). (e) Temperature-dependent PL decay time of a multi-stage, coevaporated CIGSe absorber layer. (For interpretation of the references to colour in this figure legend, the reader is referred to the web version of this article.)

(Bothe et al., 2002). To spectrally resolve the images, a tunable filter is located in front of the camera. As a result, a set of images can be collected as a function of emission energy, which can be schematically visualized in a data-cube as shown in Fig. 10a.

As an example, spectrally resolved photoluminescence images for a CIGSe thin film (the corresponding solar cells exhibit conversion efficiencies of about 16%) grown by multi-stage evaporation (Heinemann et al., 2017) can be seen in Fig. 10. Data are shown at emission energies of 1.15 eV (Fig. 10b) and 1.00 eV (Fig. 10c). The sample has been illuminated with two 660 nm lasers coupled to optical homogenizer units with an illumination power equivalent to 1 sun. The image acquired at 1.15 eV shows uniform emission throughout the whole area of the solar cell, whereas the image acquired at 1.00 eV clearly shows spatial inhomogeneities. Fig. 10d gives the PL spectra of the imaged CIGSe solar cell integrated over a bright area (black circle in Fig. 10c) and over a dark area (red circle in Fig. 10c) illustrating the spatial inhomogeneities in the PL intensity between the two regions. To be able to differentiate spatial inhomogeneities in different regions of the spectra is a great advantage for advanced analysis of the photoluminescence data. For example, the low energy side of the PL spectra can be studied to provide useful information about band tailing and electrostatic/potential fluctuations (see, e.g., references Yakushev et al. (2015), Márquez-Prieto et al. (2017). However, this analysis needs to be performed carefully since the PL spectra can be heavily distorted due to interference effects (Larsen et al., 2015).

In addition to spatial-mapping of the luminescence, the hyperspectral PL data yields information regarding quasi-fermi level splitting ($\Delta\mu$) when the system is calibrated to detect the sample emission in absolute photons (Rau and Werner, 2004; Redinger et al., 2016; Redinger and Unold, 2018). This is particularly useful under 1 sun illumination conditions, as $\Delta\mu$ represents the maximum achievable open-circuit voltage on an equivalent device, however, without the need for device completion. All-optical quantification of such device parameters is highly-desirable for material and process optimization. For the CIGSe device shown in Fig. 10, quantification of $\Delta\mu$ from the high energy slope yields 702 mV, which is in good agreement with the open-circuit voltage measured on the device of about 680 mV.

An additional optical spectroscopy technique that is useful for characterizing CIGSe absorbers and devices is time-resolved photoluminescence (TRPL). In general, TRPL is used to study carrier dynamics and quantify absorber quality, with the minority carrier lifetime τ_n commonly reported from the characteristic decay time of the PL emission τ_{PL}. However, interpreting the PL decay as the minority carrier lifetime can by controversial in CIGSe (Hages et al., 2017; Redinger et al., 2017; Maiberg et al., 2015) as the PL decay is also affected by mechanisms such as charge-carrier trapping and degradation. Additionally, graded band structures further complicate interpretation of the PL decay time as carrier drift and surface-related recombination mechanisms are quite sensitive to the absorber energy band structure.

To verify the origin of the characteristic PL decay time as well as minority carrier lifetime in CIGSe, we use a combination of temperature-dependent TRPL and quantitative PL imaging data. First, temperature dependent TRPL is used to verify the rate-limiting mechanism of the PL decay. The characteristic PL decay time for a CIGSe absorber (the corresponding solar cells exhibit conversion efficiencies of about 16%) grown by multi-stage evaporation (Hages et al., 2017) is shown in Fig. 10e between 100 and 400 K. For this absorber, room-temperature PL decay times of about 80 ns are measured, with a temperature

dependence of $\tau_{PL} \propto T^{-1.1}$; this behavior is in excellent agreement with the expected-temperature dependence of SRH-recombination (Hages et al., 2017). In contrast, a significantly stronger temperature-dependence of the PL decay time may be the result of minority carrier-trapping (Hages et al., 2017; Redinger et al., 2017; Maiberg et al., 2015) or sample degradation (Redinger et al., 2017). In the case of minority carrier-trapping, the PL decay time cannot be interpreted as the minority carrier lifetime. To investigate further the minority carrier lifetime in CIGSe – in cases where the PL decay time does not reflect recombination or to further verification of the minority carrier lifetime is needed – the steady-state PL yield can be used, obtained from the quantitative PL imaging previously described. The value of τ_n can be estimated from the internal PL efficiency η_{PL} in low-injection from $\tau_n = \eta_{PL}/Bp_0$, where B is the radiative coefficient and p_0 is the absorber doping (Hages et al., 2017). For the CIGSe absorbers shown in Fig. 10d, the external PL yield of 0.2% is the result of a minority carrier lifetime of about 400 ns, which is in good agreement with TRPL data on these absorbers – demonstrating that the long PL decay time measured is indeed related to the minority carrier lifetime. In general, for the PL decay time to be interpreted as the minority carrier lifetime, the TRPL, the steady-state PL efficiency, and temperature-dependence of the PL decay need to be in good agreement.

7. Summary and outlook

The present overview article provided insight into in-situ growth monitoring of CIGSe absorber layers as well as various approaches applied at HZB for studying bulk properties and surfaces of individual layers and also completed solar-cell stacks, on scales from mm down to nm. It was shown that the combination of in-situ analysis methods can be used to investigate correlations of extended structural defects (such as stacking faults) with optoelectronic properties. Complementary, ex-situ analysis of structural properties via X-ray or neutron diffraction techniques gives the means to confirm (micro)structural film properties and to obtain information on point defects, while a combination of XPS, XES, UPS, and IPES allows for analyzing chemical and electronic structures of surfaces and interfaces in solar-cell stacks. In order to detect elemental distributions in the solar-cell stack or fluctuations in the optoelectronic properties of CIGSe absorber layers, electron microscopy can give corresponding insight, which is complemented by optical spectroscopy providing information on, e.g., charge-carrier lifetimes. In spite of the diverse information already accessed by the methods described in the present work, still, additional work involving, e.g., materials and multidimensional device modelling performed by external partners is needed in order to assist the correlation of materials properties with the device performance.

Acknowledgements

The authors are grateful for financial support by the Helmholtz Virtual Institute “Microstructure Control for Thin-Film Solar Cells” (VH-VI-520), by the BMWi projects SpeedCIGS and EFFCIS, as well as by the Impuls- und Vernetzungsfonds of the Helmholtz-Association (VH-NG-423). AR acknowledges funding by the Fonds national de la recherché, Luxembourg, and RC financial support from Spanish MINECO within the Ramón y Cajal program (RYC-2011-08521).

References

Abou-Ras, D., Schäfer, N., Baldaz, N., Brunken, S., Boit, C., 2015. Electron-beam-induced current measurements with applied bias provide insight to locally resolved acceptor concentrations at p-n junctions. AIP Adv. 5, 077191-1–7.

D. Abou-Ras, M. Nichterwitz, M. Romero, S.S. Schmidt, Electron microscopy on thin films for solar cells, ch. 14, in D. Abou-Ras, T. Kirchartz, and U. Rau, (Eds.), Advanced Characterization Techniques for Thin Film Solar Cells, volume 1. (Wiley-VCH, Berlin, 2016).

Abou-Ras, D., Schäfer, N., Rissom, T., Kelly, M.N., Haarstrich, J., Ronning, C., Rohrer, G.S., Rollett, A.D., 2016b. Grain-boundary character distribution and correlations with electrical and optoelectronic properties of $CuInSe_2$ thin films. Acta Mater. 118, 244–252.

Abou-Ras, D., Schmidt, S.S., Schäfer, N., Kavalakkatt, J., Rissom, T., Unold, T., Mainz, R., Weber, A., Kirchartz, T., Simsek Sanli, E., van Aken, P.A., Ramasse, Q.M., Kleebe, H.-J., Azulay, D., Balberg, I., Millo, O., Cojocaru-Mirédin, O., Barragan-Yani, D., Albe, K., Haarstrich, J., Ronning, C., 2016c. Compositional and electrical properties of line and planar defects in $Cu(In,Ga)Se_2$ thin films for solar cells - a review. Phys. Status Solidi (RRL) 10, 363–375.

Abou-Ras, D., Schäfer, N., Hages, C.J., Levcenko, S., Marquez, J., Unold, T., 2018. Inhomogeneities in $Cu(In,Ga)Se_2$ thin films for solar cells: band-gap versus potential fluctuations. RRL Solar 2, 1700199.

Alonso, M.I., Wakita, K., Pascual, J., Garriga, M., Yamamoto, N., 2001. Optical functions and electronic structure of $CuInSe_2$, $CuGaSe_2$, $CuInS_2$, and $CuGaS_2$. Phys. Rev. B 63, 075203.

Attenuation length calculated by http://henke.lbl.gov/optical_constants/atten2.html, which is based on B.L. Henke, E.M. Gullikson, J.C. Davis, X-ray interactions: photoabsorption, scattering, transmission, and reflection at E = 50-30000 eV, Z = 1-92, Atomic Data and Nuclear Data Tables 54 (1993) 181–342.

Collaboration: Authors and editors of the volumes III/17H-17I-41E: In_2S_3 energy gaps, interband transition energies. Madelung, O., Rössler, U., Schulz, M. (ed.). Springer Materials – The Landolt-Börnstein Database (http://www.springermaterials.com). http://dx.doi.org/10.1007/10717201_823.

Baier, R., Abou-Ras, D., Rissom, T., Lux-Steiner, M.C., Sadewasser, S., 2011. Symmetry-dependence of electronic grain boundary properties in polycrystalline $CuInSe_2$ thin films. Appl. Phys. Lett. 99, 172102-1–3.

M. Bär, S. Nishiwaki, L. Weinhardt, S. Pookpanratana, O. Fuchs, M. Blum, W. Yang, J. D. Denlinger, W. N. Shafarman, C. Heske, Depth-resolved band gap energies in Cu(In, Ga)(S, Se)2 thin films, Appl. Phys. Lett. 2008, 93, 244103-1-3.

Bär, M., Repins, I., Contreras, M.A., Weinhardt, L., Noufi, R., Heske, C., 2009. Chemical and electronic surface structure of 20%-efficient $Cu(In,Ga)Se_2$ thin film solar cell absorbers. Appl. Phys. Lett. 95 052106-1-3.

Bär, M., Barreau, N., Couzinié-Devy, F., Pookpanratana, S., Klaer, J., Blum, M., Zhang, Y., Yang, W., Denlinger, J.D., Schock, H.-W., Weinhardt, L., Kessler, J., Heske, C., 2010. Non-destructive depth-resolved spectroscopic investigation of the heavily intermixed In_2S_3/$Cu(In,Ga)Se_2$ interface. Appl. Phys. Lett. 96, 184101-1–3.

M. Bär, N. Barreau, F. Couzinié-Devy, R. Félix, J. Klaer, S. Pookpanratana, M. Blum, Y. Zhang, J.D. Denlinger, W. Yang, R.G. Wilks, L. Weinhardt, H.-W. Schock, J. Kessler, C. Heske, The heavily intermixed In2S3/$Cu(In,Ga)Se_2$ interface as revealed by photo- and x-ray emission spectroscopy, Proc. 39th IEEE Photovoltaic Specialists Conference, Tampa, FL, USA, June 16–21, 2013, p. 857–862.

M. Bär, L. Weinhardt, C. Heske, Soft X-Ray and Electron Spectroscopy: A Unique Tool Chest to Characterize the Chemical and Electronic Properties of Surfaces and Interfaces, ch. 18, in D. Abou-Ras, T. Kirchartz, and U. Rau, (Eds.), Advanced Characterization Techniques for Thin Film Solar Cells, volume 2. (Wiley-VCH, Berlin, 2016).

Bär, M., Barreau, N., Couzinié-Devy, F., Weinhardt, L., Wilks, R.G., Kessler, J., Heske, C., 2016b. Impact of annealing-induced intermixing on the electronic level alignment at the In_2S_3/$Cu(In,Ga)Se_2$ thin-film solar cell interface - or why significant intermixing allows for high efficiencies. ACS Appl. Mater. Interf. 8, 2120–2124.

N. Barreau, Sol. Energy, Indium sulfide and relatives in the world of photovoltaics, 83, (2009) 363–371.

Barreau, N., Deudon, C., Lafond, A., Gall, S., Kessler, J., 2006. A study of bulk $Na_xCu_{1-x}In_5S_8$ and its impact on the $Cu(In,Ga)Se_2$/In_2S_3 interface of solar cells. Sol. Energy Mater. Sol. Cells 90, 1840–1848.

Bothe, K., Bauer, G.H., Unold, T., 2002. Spatially resolved photoluminescence measurements on $Cu(In,Ga)Se_2$ thin films. Thin Solid Films 403–404, 453–456.

Contreras, M.A., Romero, M.J., Noufi, R., 2006. Characterization of $Cu(In,Ga)Se_2$ materials used in record performance solar cells. Thin Solid Films 511–512, 51–54.

Gunder, R., Marquardt, J., Leppin, L., Schorr,S., 2017. Microstructure analysis of chalcopyrite-type CuInSe2 and kesterite-type Cu2ZnSnSe4 absorber layers in thin film solar cells, ch. 4. In: Heuss-Aßbichler, S., Amthauer, G., John, M. (Eds.), Highlights in Applied Mineralogy (de Gruyter, 2017), pp. 73–97 http://dx.doi.org/10.1515/9783110497342-004.

Hages, C.J., Redinger, A., Levcenko, S., Hempel, H., Koeper, M.J., Agrawal, R., Greiner, D., Kaufmann, C.A., Unold, T., 2017. Identifying the real minority carrier lifetime in nonideal semiconductors: a case study of kesterite materials. Adv. Energy Mater. 18, 1700167.

Hauschild, D., Meyer, F., Benkert, A., Kreikemeyer-Lorenzo, D., Pohlner, S., Palm, J., Blum, M., Yang, W., Wilks, R.G., Bär, M., Heske, C., Weinhardt, L., Reinert, F., 2015. Annealing-induced effects on the chemical structure of the In_2S_3/$CuIn(S,Se)_2$ thin-film solar cell interface. J. Phys. Chem. C 119, 10412–10416.

Hauschild, D., Meyer, F., Benkert, A., Kreikemeyer-Lorenzo, D., Dalibor, T., Palm, J., Blum, M., Yang, W., Wilks, R.G., Bär, M., Reinert, F., Heske, C., Weinhardt, L., 2018. Improving performance by Na doping of a buffer layer – chemical and electronic structure of the InxSy:Na/CuIn(S, Se)2 thin-film solar cell interface. Prog. Photovolt. http://dx.doi.org/10.1002/pip.2993 (in press).

Heinemann, M.D., Mainz, R., Österle, F., Rodriguez-Alvarez, H., Greiner, D., Kaufmann, C.A., Unold, T., 2017. Evolution of opto-electronic properties during film formation of complex semiconductors. Sci. Rep. 7, 45463.

Kühnapfel, S., Gall, S., Sonntag, P., Schäfer, N., Abou-Ras, D., 2016. Direct correlation of microstructure and device performance of liquid phase crystallized Si thin film solar cells on glass. Phys. Stat. Sol. (RRL) 10, 657–661.

Larsen, J.K., Li, S.Y., Scragg, J.J.S., Ren, Y., Hägglund, C., Heinemann, M.D., Kretzschmar, S., Unold, T., Platzer-Björkman, C., 2015. Interference effects in photoluminescence spectra of Cu_2ZnSnS_4 and $Cu(In,Ga)Se_2$ thin films. J. Appl. Phys. 118, 035307.

Le Bail, Duroy, H., Fourquet, J.L., 1988. Ab-initio structure determination of $LiSbWO_6$ by X-ray powder diffraction. Mater. Res. Bull. 23, 447–452.
Liu, X., Sites, J.R., 1996. Calculated effect of conduction-band offset on $CuInSe_2$ solar-cell performance. AIP Conf. Proc. 353, 444–452.
Maiberg, M., Hölscher, T., Zahedi-Azad, S., Fränzel, W., Scheer, R., 2015. Investigation of long lifetimes in $Cu(In,Ga)Se_2$ by time-resolved photoluminescence. Appl. Phys. Lett. 107, 122104.
Mainz, R., Rodriguez-Alvarez, H., Klaus, M., Thomas, D., Lauche, J., Weber, A., Heinemann, M.D., Brunken, S., Greiner, D., Kaufmann, C.A., Unold, T., Schock, H.-W., Genzel, C., 2015. Sudden stress relaxation in compound semiconductor thin films triggered by secondary phase segregation. Phys. Rev. B 92, 155310.
Mainz, R., Simsek Sanli, E., Stange, H., Azulay, D., Brunken, S., Greiner, D., Hajaj, S., Heinemann, M.D., Kaufmann, C.A., Klaus, M., Ramasse, Q.M., Rodriguez-Alvarez, H., Weber, A., Balberg, I., Millo, O., van Aken, P.A., Abou-Ras, D., 2016. Annihilation of structural defects in chalcogenide absorber films for high-efficiency solar cells. Energy Environ. Sci. 9, 1818–1827.
Márquez-Prieto, J., Yakushev, M.V., Forbes, I., Krustok, J., Edwards, P.R., Zhivulko, V.D., Borodavchenko, O.M., Mudryi, A.V., Sulimov, M., Dimitrievska, M., Izquerdo-Roca, V., Pearsall, N.M., Martin, R.W., 2017. Influence of the copper content on the optical properties of CZTSe thin films. Sol. Energy Mater. Sol. Cells 168, 69–77.
Minemoto, T., Matsui, T., Takakura, H., Hamakawa, Y., Negami, T., Hashimoto, Y., Uenoyama, T., Kitagawa, M., 2001. Theoretical analysis of the effect of conduction band offset of window/CIS layers on performance of CIS solar cells using device simulation. Sol. Energy Mater. Sol. Cells 67, 83–88.
Morkel, M., Weinhardt, L., Lohmüller, B., Heske, C., Umbach, E., Riedl, W., Zweigart, S., Karg, F., 2001. Flat conduction band alignment at the $CdS/CuInSe_2$ thin film solar cell heterojunction. Appl. Phys. Lett. 79, 4482–4484.
Nichterwitz, M., Abou-Ras, D., Sakurai, K., Bundesmann, J., Unold, T., Scheer, R., Schock, H.W., 2009. Influence of grain boundaries on current collection in $Cu(In,Ga)Se_2$ thin-film solar cells. Thin Solid Films 517, 2554–2557.
Niemegeers, A., Burgelman, M., de Vos, A., 1995. On the $CdS/CuInSe_2$ conduction band discontinuity. Appl. Phys. Lett. 67, 845–847.
Oliva, F., Kretzschmar, S., Colombara, D., Tombolato, S., Ruiz, C.M., Redinger, A., Saucedo, E., Broussillou, C., de Monsabert, T.G., Unold, T., Dale, P.J., Izquierdo-Roca, V., Pérez-Rodríguez, A., 2016. Optical methodology for process monitoring of chalcopyrite photovoltaic technologies: application to low cost $Cu(In,Ga)(S,Se)_2$ electrodeposition based processes. Sol Energy Mater. Sol. Cells 158, 168–183.
Pistor, P., Zahedi-Azad, S., Hartnauer, S., Wägele, L. A., Jarzembowski, E., Scheer, R., 2015. Real time observation of phase formations by XRD during Ga-rich or In-rich Cu $(In,Ga)Se_2$ growth by co-evaporation. Phys. Status Solidi (a) 212, 1897–1904.
Pistor, P., Mainz, R., Heinemann, M.D., Unold, T., Scheer, R., 2016. In situ real-time characterization of thin-film growth. In: Abou-Ras, D., Kirchartz, T., Rau, U. (Eds.), Advanced Characterization Techniques for Thin Film Solar Cells, vol. 2. Wiley-VCH, Berlin (Chapter 16).
Pohl, J., Albe, K., 2010. Thermodynamics and kinetics of the copper vacancy in $CuInSe_2$, $CuGaSe_2$, $CuInS_2$, and $CuGaS_2$ from screened-exchange hybrid density functional theory. J. Appl. Phys. 108, 023509.
Press release Solar Frontier, Solar Frontier Achieves World Record Thin-Film Solar Cell Efficiency of 22.9%. < http://www.solar-frontier.com/eng/news/2017/1220_press.html > (accessed on March 28, 2018).
Press release Solar Frontier, Solar Frontier's CIS Thin-Film Submodule Achieves Highest Efficiency World Record of 19.2%. < http://www.solar-frontier.com/eng/news/2017/0227_press.html > (accessed on March 28, 2018).
QUASES-IMFP-TPP2M Ver. 3.0 code: Inelastic electron mean free paths calculated from the TPP-2M formula based on S. Tanuma, C. J. Powell, D. R. Penn, Calculations of electron inelastic mean free paths. V. Data for 14 organic compounds over the 50–2000 eV range, Surf. Interf. Anal. 21 (1994) 165–176 and H. Shinotsuka, S. Tanuma, C. J. Powell, D. R. Penn, Calculations of electron inelastic mean free paths. X. Data for 41 elemental solids over the 50 eV to 200 keV range with the relativistic full Penn algorithm, Surf. Interf. Anal. 47 (2015) 871–888.
Rau, U., Werner, J.H., 2004. Radiative efficiency limits of solar cells with lateral band-gap fluctuations. Appl. Phys. Lett. 84, 3735–3737.
Redinger, A., Unold, T., 2018. High surface recombination velocity limits Quasi-Fermi level splitting in kesterite absorbers. Sci. Rep. 8, 1874.
Redinger, A., Kretzschmar, S., Unold,T., 2016. Quantitative PL Imaging of thin film solar cells – potential and pitfalls. In: Proc. 43rd IEEE Photovoltaic Specialists Conference, Portland, OR, June 05–10, pp. 3559–3562.
Redinger, A., Levcenko, S., Hages, C.J., Greiner, D., Kaufmann, C.A., Unold, T., 2017. Time resolved photoluminescence on $Cu(In,Ga)Se_2$ absorbers: distinguishing degradation and trap states. Appl. Phys. Lett. 110, 122104.
Rietveld, H.M., 1967. Line profiles of neutron powder-diffraction peaks for structure refinement. Acta Cryst. 22, 151–152.
Rockett, A.A., 2005. The effect of Na in polycrystalline and epitaxial single-crystal $CuIn_{1-x}Ga_xSe_2$. Thin Solid Films 480, 2–7.
Rodriguez-Alvarez, H., Weber, A., Lauche, J., Kaufmann, C.A., Rissom, T., Greiner, D., Klaus, M., Unold, T., Genzel, C., Schock, H.-W., Mainz, R., 2013a. Formation of $CuInSe_2$ and $CuGaSe_2$ thin-films deposited by three-stage thermal co-evaporation: a real-time X-ray diffraction and fluorescence study. Adv. Energy Mater. 3, 1381–1387.
Rodriguez-Alvarez, H., Barreau, N., Kaufmann, C., Weber, A., Klaus, M., Painchaud, T., Schock, H.-W., Mainz, R., 2013b. Recrystallization of $Cu(In,Ga)Se_2$ thin films studied by X-ray diffraction. Acta Mater. 61, 4347–4353.
Rudmann, D., 2004. Effects of sodium on growth and properties of Cu(In, Ga)Se2 thin films and solar cells. Ph.D. thesis. ETH Zurich.
Schäfer, N., Winkelmann, A., Wilkinson, A.J., Schmid, T., Schülli, T.U., Chahine, G.A., Marquardt, J., Schorr, S., Klaus, M., Genzel, C., Rissom, T., Abou-Ras, D., 2016. Microstrain distribution mapping on $CuInSe_2$ thin films by means of electron backscatter diffraction, X-ray diffraction, and Raman microspectroscopy. Ultramicroscopy 169, 89–97.
Schmid, D., Ruckh, M., Grunwald, F., Schock, H.-W., 1993. Chalcopyrite/defect chalcopyrite heterojunctions on the basis of $CuInSe_2$. J. Appl. Phys. 73, 2902–2909.
Schorr, S., Stephan, C., Törndahl, T., Gunder, R., Többens, D., 2016. X-ray and neutron diffraction on materials for thin-film solar cells. In: Abou-Ras, D., Kirchartz, T., Rau, U. (Eds.), Advanced Characterization Techniques for Thin Film Solar Cells, vol. 1. Wiley-VCH, Berlin (Chapter 15).
Simsek Sanli, E., Barragan-Yani, D., Ramasse, Q.M., Mainz, R., Abou-Ras, D., Weber, A., Kleebe, H.-J., Albe, K., van Aken, P.A., 2017. Point defect segregation at Frank loops in $Cu(In,Ga)Se_2$ thin-film absorbers. Phys. Rev. B 95, 195209.
Song, X., Caballero, R., Félix, R., Gerlach, D., Kaufmann, C.A., Schock, H.-W., Wilks, R.G., Bär, M., 2012. Na incorporation into $Cu(In,Ga)Se_2$ thin-film solar cell absorbers deposited on polyimide: impact on the chemical and electronic surface structure. J. Appl. Phys. 111, 034903.
Stange, H., Brunken, S., Hempel, H., Rodriguez-Alvarez, H., Schäfer, N., Greiner, D., Scheu, A., Lauche, J., Kaufmann, C.A., Unold, T., Abou-Ras, D., Mainz, R., 2015. Effect of Na presence during $CuInSe_2$ growth on stacking fault annihilation and electronic properties. Appl. Phys. Lett. 107, 152103.
Stange, H., Brunken, S., Greiner, D., Heinemann, M.-D., Kaufmann, C.A., Schmidt, S.S., Bäcker, J.-P., Klaus, M., Genzel, C., Mainz, R., 2016. Diffusion-induced grain boundary migration as mechanism for grain growth and defect annihilation in chalcopyrite thin films. Acta Mater. 111, 377–384.
Stephan, C., Scherb, T., Kaufmann, C.A., Schorr, S., Schock, H.-W., 2012. Cationic point defects in $CuGaSe_2$ from a structural perspective. Appl. Phys. Lett. 101, 101907.
Stephan, C., Schorr, S., Tovar, M., Schock, H.-W., 2011. Comprehensive insights into point defect and defect cluster formation in $CuInSe_2$. Appl. Phys. Lett. 98, 091906.
Stephan, C., Greiner, D., Schorr, S., Kaufmann, C.A., 2016. The influence of sodium on the point defect characteristics in off stoichiometric $CuInSe_2$. J. Phys. Chem. Solids 98, 309–315.
Treacy, M.M.J., Newsam, J.M., Deem, M.W., 1991. A general recursion method for calculating diffracted intensities from crystals containing planar faults. Proc. R. Soc. Lond. A 433, 499–520.
Tuttle, J.R., Albin, D.S., Noufi, R., 1991. Thoughts on the microstructure of polycrystalline thin film $CuInSe_2$ and its impact on material and device performance. Sol. Cells 30, 21–38.
Unold, T., Gütay, L., 2016. Photoluminescence analysis of thin-film solar cells ch. 11. In: Abou-Ras, D., Kirchartz, T., Rau, U. (Eds.), Advanced Characterization Techniques for Thin Film Solar Cells, vol. 1. Wiley-VCH, Berlin.
Wei, S.-H., Zunger, A., 1995. Band offsets and optical bowings of chalcopyrites and Zn-based II-VI alloys. J. Appl. Phys. 78, 3846–3856.
Yakushev, M.V., Márquez-Prieto, J., Forbes, I., Edwards, P.R., Zhivulko, V.D., Mudryi, A.V., Krustok, J., Martin, R.W., 2015. Radiative recombination in $Cu_2ZnSnSe_4$ thin films with Cu deficiency and Zn excess. J. Phys. D: Appl. Phys. 48, 475109.
Zhang, S.B., Wei, S.-H., Zunger, A., Katayama-Yoshida, H., 1998. Defect physics of the $CuInSe_2$ chalcopyrite semiconductor. Phys. Rev. B 57, 9642–9656.